Revisiting Queney's Flow Over a Mesoscale Ridge

David J Muraki [1]

Simon Fraser University, Burnaby BC, CANADA

[1]Corresponding Author: David J Muraki, Department of Mathematics, Simon Fraser University, Burnaby BC V5A 1S6, CANADA. e-mail: muraki@math.sfu.ca

Abstract

The most familiar illustrations of downstream topographic waves are the streamline plots from the original linear wave studies of Queney. For steady flow past a two-dimensional ridge, Queney's downstream radiation patterns were obtained through approximations of the Fourier integral which describes the dispersion of linear gravity waves. In the case of constant stratification with rotation, a high-accuracy numerical quadrature of the Fourier integral reveals significant departures in the near-ridge streamfunction pattern from the original depictions. This numerical accuracy is achieved by a specialized quadrature scheme for computing the singular Fourier integrals encountered in this regime of order-one Rossby number. In addition, a *steepest descent* approximation is presented which resolves the breakdown of Queney's analysis above of the summit and quantifies the unusually weak decay of wave amplitude with height.

1. Introduction

The foundations for our understanding of atmospheric wave generation by mesoscale topography were established in the linear analyses of Queney (1947, 1948) for steady flow past a two-dimensional ridge. In these seminal works, downstream radiation patterns were inferred from the dispersion characteristics of linear gravity waves. Queney's 1948 streamline figures, based upon approximations to a Fourier integral, are frequently reproduced in reviews and texts and are recognized as the canonical illustration of downstream topographic waves. Specifically in the case of constant stratification with rotation, we have noted significant departures in the near-ridge streamfunction pattern between the original approximation (Queney 1948, Figure 3) and direct quadrature of the Fourier integral. Of the cases studied by Queney, the one with rotation is most problematic as the Fourier integral is singular at the inertial wavenumber. Surprisingly, it seems that there is little awareness of this discrepancy, despite that accurate computations have occasionally appeared in the literature (Durran & Klemp 1983, Pierrehumbert 1986, Garner 1999). [1] Here we present an updated study for steady topographic waves in a rotating, stratified, hydrostatic flow.

In this rethinking of the Queney problem for order-one Rossby number, several new analytical tools for understanding linear topographic waves have been developed. The first is a highly accurate quadrature scheme for the Fourier integral. Our approach to the Fourier integration abandons the usually efficient fast-Fourier transform, and directly addresses the resolution of the inertial singularity. Although the implementation described here is specific to the two-dimensional ridge, similar methodologies are adaptable to the case of three-dimensional, linear flow around mountain topography, where both the nonrotating and rotating cases yield singular Fourier integrals. In the latter case (order-one Rossby number), steady flows from direct quadrature of the three-dimensional Fourier integral have yet to

[1] Subtle discrepancies discovered during model development are still being reported; one instance as recently as (Hsu, et.al. 2001) for the non-rotating, non-hydrostatic case.

appear in the literature. The second is a *steepest descent* approximation to the Fourier integral which produces a remarkably uniform representation of the solution that resolves the breakdown in Queney's (1947) analysis at the summit zenith. This new approximation obtains a formula for the slow vertical decay of the mountain waves, and also suggests that a weak, near-inertial wave is produced by back-scattering from the downslope surface. The last is a set of surface formulas which connects these finite Rossby number wave flows with the zero Rossby number quasigeostrophic (QG) flow. These formulas complement previous surface results of Bretherton (1969) and Pierrehumbert (1984).

2. The Linearized Wave Problem

The fluid dynamical setting considered by Queney was the steady, linearized equations for an incompressible, Boussinesq atmosphere in two dimensions x, z. The flow is assumed to be rotating (f-plane) and hydrostatic, and to have constant stratification. Under these assumptions, the linear primitive equations are

$$\begin{aligned} u_x &+ w_z &&= 0 \\ U\,u_x &- f\,v &&= -\rho_0^{-1}\,p_x \\ U\,v_x &+ f\,u &&= 0 \\ & 0 &&= -\rho_0^{-1}\,p_z + b \\ U\,b_x &+ N^2\,w &&= 0 \end{aligned} \tag{1}$$

where the winds are denoted by u, v, the vertical motion by w, buoyancy anomaly by b, and pressure by p. The external parameters are: incident wind U, Coriolis parameter f, Brünt-Vaisala frequency N and mean density ρ_0. The linearized topographic boundary condition for a no-normal flow surface $z = h(x)$ is

$$w = U\,h_x \quad \text{at} \quad z = 0\ . \tag{2}$$

Lastly, decay or outward wave radiation conditions are imposed on the linear modes in the far-field.

The primitive equations (1) can be manipulated into a single equation involving only the buoyancy anomaly $b(x,z)$

$$k_s^2\, b_{xx} + k_f^2\, b_{zz} + b_{xxzz} = 0 \tag{3}$$

where the Scorer parameter, $k_s = N/U$, and inertial wavenumber, $k_f = f/U$, are coefficients associated with stratification and rotation. Within this linear limit, the topographic condition (2) is equivalent to a buoyancy condition on the surface so that $b(x,0) = -N^2\, h(x)$. The Fourier integral solution of (3) is

$$b(x,z) = -\frac{N^2}{\pi}\ \mathrm{Re}\left\{ \int_0^\infty \hat{h}(k)\ e^{ikx}\ e^{im(k)z}\ dk \right\} \tag{4}$$

where $\hat{h}(k)$ is the Fourier transform of the topography

$$\hat{h}(k) = \int_{-\infty}^{+\infty} h(x)\ e^{-ikx}\ dx \tag{5}$$

(Queney 1947, p64). The linear dispersion relation for the buoyancy anomaly equation (3)

$$k_s^2\, k^2 + k_f^2\, m^2 - k^2\, m^2 = 0 \tag{6}$$

determines the vertical mode number $m(k)$

$$m(k) = \begin{cases} \dfrac{i\, k_s\, k}{\sqrt{k_f^2 - k^2}} & \text{for} \quad 0 \le k < k_f \\ \\ \dfrac{k_s\, k}{\sqrt{k^2 - k_f^2}} & \text{for} \quad k_f < k < +\infty \end{cases} \tag{7}$$

where the sign choices of $m(k)$ embody the far-field conditions at $z \to +\infty$ (Pierrehumbert 1984). The long waves ($0 \le k < k_f$) decay as $z \to +\infty$, and the short waves ($k_f < k < +\infty$) radiate energy upward.

3. Streamline Comparisons

As in Queney's original work, we focus on a particular choice of topography, the so-called *Witch of Agnesi*, or bell-shaped ridge

$$h(x) = \frac{HL^2}{L^2 + x^2} \qquad ; \qquad \hat{h}(k) = \pi\, HL\; e^{-|k|L} \tag{8}$$

as a representative profile for an isolated ridge with height H and horizontal length scale L. The buoyancy solution (4) specific to the above ridge (8) is

$$b(x,z) = -\,N^2 H\ \mathrm{Re}\Big\{ \int_0^\infty e^{(ix-L)\,k}\; e^{im(k)z}\; L dk \Big\} = -\,N^2 H\ \mathrm{Re}\{I(x,z)\} \tag{9}$$

which defines the Fourier integral $I(x,z)$. The total buoyancy field, including the background stratification, is given by

$$b^T(x,z) = N^2\, z + b(x,z)\ , \tag{10}$$

so that contours of $b^T(x,z)$ correspond to the steady streamlines of the flow over the ridge. Conveniently, this bell-shaped topographic ridge (8) also has an exact QG solution (Smith 79a; Gill 1982, p282)

$$b^{QG}(x,z) = -\,N^2 H \left\{ \frac{k_f L\,(k_f L + k_s z)}{(k_f L + k_s z)^2 + (k_f x)^2} \right\} \tag{11}$$

which satisfies just the second-order terms of (3). This QG solution describes the fore-aft symmetric uplifting of the flow over the ridge and is devoid of waves.

Queney's figure (1948, p22) is reproduced here as Figure 1a with the ridge parameters $H = 1$ km and $L = 100$ km chosen for unity Rossby and Froude numbers

$$\mathcal{R} \equiv \frac{U}{f\,L} = \frac{1}{k_f L} = 1 \qquad ; \qquad \mathcal{F} \equiv \frac{U}{N\,H} = \frac{1}{k_s H} = 1\ . \tag{12}$$

The streamlines $z^Q(x)$ in the Queney's figure are the approximate inversion of (10) based upon vertical displacement

$$z^Q(x) = z^\infty - \frac{1}{N^2}\, b(x, z^\infty) \tag{13}$$

which is obtained by integrating the vertical motion along a fixed height z^{∞}. Although these displacement streamlines only approximate the true streamlines (steady isentropes), their use is consistent within the linear limit of large Froude number. Figure 1b represents a recalculation of the displacement streamlines (13) by direct quadrature of the Fourier integral (9) at parameter values (12). The details of the high-order numerical scheme used in the quadrature of the Fourier integral $I(x, z)$ are deferred to Appendix A.

Although the original Queney figure captures the essential features of the wave flow, there are several noteworthy shortcomings that become apparent in the quadrature solution of Figure 1b. Above the ridge summit, the computed pattern of wavecrests is much more regular than originally rendered. This is especially the case at lower altitudes, where the first maxima of upward displacement clearly occur upstream of the ridge summit, and there is a distinct phaseline of abrupt downdrafts associated with strong downslope winds. These features are common to the non-rotating cases of Queney. In the downstream wake, the quadrature streamlines show a mean upward displacement. This upward tendency is a vestige of the quasigeostrophic response (11) to the topography. Also, the streamline oscillations decay more slowly downstream and persist much closer to the surface than is suggested in Queney's figure. This is consistent with the analysis of Pierrehumbert (1984) which indicates a gradual $x^{-1/2}$ decay of the oscillations in the surface winds u and v. Overall, the features in Figure 1b are in complete agreement with Pierrehumbert (1986).

The discrepancies between Figures 1a and 1b are not unexpected given the nature of Queney's (1947) approximations. The far-field oscillations are in good agreement, as they are obtained from stationary phase formulas which are asymptotically valid for large $x, z > 0$ (Queney 1947, equation 119). The stationary phase method also gives a QG response in the far-field upstream (Queney 1947, equation 121). If Queney had included this effect symmetrically on the downstream side as well, the upward tendency of the streamlines in the lee would have been correctly incorporated. The remaining descrepancies stem from

the difficulties Queney encountered in the two transition zones where the stationary phase method could not be applied: the zenith direction aloft ($x \approx 0$), and the near-surface downstream ($z \approx 0$). As will be discussed in Section 5, this breakdown of the stationary phase analysis can be partially circumvented by the use of the steepest descent approximation.

4. Linearized Flow Plots

As a benchmark of linearized theory, solution fields for the associated disturbance quantities are presented in Figures 2a-d: buoyancy anomaly (b), vertical motion (w), across- and along-ridge winds (u, v). These flow quantities are related to the buoyancy integral (4) through differentiations and integrations

$$w = -\frac{U}{N^2}\, b_x \qquad ; \qquad u = \frac{U}{N^2}\, b_z \qquad ; \qquad v_x = -\frac{f}{U}\, u \ , \tag{14}$$

for which the corresponding Fourier integral expressions are easily derived. Quadrature of these quantities using the desingularization strategy of Appendix A is also straightforward. Figures 2a-d are computed for unity Rossby number ($\mathcal{R} = 1.0$), but are independent of Froude number up to a scaling of the topographic height H. Hence, the only Froude number dependent aspect of these figures is the shaded ridge topography (for $\mathcal{F} = 3$), which is included for visual reference only.

In Figure 2a (contour interval: 0.15 $N^2 H$), the cold (negative) bias of the buoyancy anomaly comes from the QG-like response (11) associated with the substantial contribution of the integral near $k = 0$. All solid contours indicate zero values and are identical to those shown in Figure 1b. Vertical motion, shown in Figure 2b (contour interval: 0.25 fH), is concentrated aloft of the ridge. This contrasts with the across- and along-ridge winds shown in Figures 2c,d (contour interval: 0.15 NH) which have greater downstream extent. These distributions of u and w are consistent with the buoyancy anomaly which also serves as their streamfunction (14). In addition, the leftmost zero contour in Figure 2c shows that the region of accelerating across-ridge flow begins a considerable distance upstream

at altitudes above the ridge height. As expected, the maximum u is associated with the downslope winds in the lee of the ridge. Also apparent in the along-ridge v flow is the asymmetry in the strengths and positions of the windward barrier jet and the jet in the lee of the ridge. A common feature of both wind plots (Figures 2c,d) are the near-inertial oscillations in the low-level winds downstream of the ridge. These structures are associated with the downstream oscillations in the surface ($z = 0$) Greens function of Pierrehumbert (1994) and are attributable to wavenumbers just above the near-inertial singularity in the integrand ($k \approx k_f$). Generally, the features in Figure 2a-d conform well with the small amplitude case of Trüb and Davies (1994, Figure 7) which is obtained by a time-relaxation of a fully nonlinear numerical model. Although not shown, our numerical quadrature at Rossby number 2.0 is in complete agreement with the careful calculation of the buoyancy anomaly (disturbance streamfunction) by Garner (1999).

5. Steepest Descent Approximation

An alternative, analytical perspective on the wave solution (9) is obtained by the method of steepest descent. In the spirit of Queney, these approximate formulas involve only elementary functions (powers and exponentials), but are well-behaved in the transition regions associated with the summit zenith and downstream surface. Figure 3 is a representation of Queney's original figure where the displacement streamlines are now obtained by steepest descent. Although this approximation cannot achieve the accuracy obtained through the direct numerical quadrature (Figure 1b), the closed-form expressions give a different quantitative insight into the Fourier solution (9).

The analysis that follows is specific to the choice of the bell-shaped ridge, but can be adapted to more general topography. The steepest descent approximation for the buoyancy integral $I(x, z)$ defined in (9) involves a three-term sum of contributions: a quasigeostrophic

response, a primary and a secondary wave

$$I(x,z) \sim I^{QG}(x,z) + I^{S1}(x,z) + I^{S2}(x,z) \ . \tag{15}$$

Explicit formulas for evaluating each of these terms are stated below, but the derivation of these three terms is deferred to Appendix B. The $I^{QG}(x,z)$ term represents a contribution from the integrand near $k = 0$, whose real part recovers the buoyancy field of quasigeostrophic theory (11)

$$I^{QG}(x,z) = \frac{k_f L}{k_s z - k_f(ix - L)} \ . \tag{16}$$

The two wave terms, $I^{S1}(x,z)$ and $I^{S2}(x,z)$, are obtained from steepest descent formulas that require careful evaluation of the multi-valued, complex functions: square and cube roots, and the complex angle (arg). These formulas involve the exponent of the integrand (9), denoted by $\phi(k)$, which is extended to complex values of k

$$\phi(k) = (ix - L)\, k + \frac{ik_s kz}{(k - k_f)^{1/2}\ (k + k_f)^{1/2}} \tag{17}$$

by defining branch cuts $-7\pi/4 < \arg(k - k_f) < +\pi/4$ and $-\pi < \arg(k + k_f) < +\pi$ that are consistent with (7). The primary wave term, $I^{S1}(x,z)$, is then obtained from the steepest descent formula

$$I^{S1}(x,z) \sim \sigma_1 \sqrt{\frac{2\pi L^2}{|\phi''(\kappa_1)|}}\ \exp\left\{\phi(\kappa_1) - i\ \arg(-\phi''(\kappa_1)/2)\right\} \ . \tag{18}$$

where $\kappa_1(x,z)$ and $\sigma_1(x,z)$ are defined below. The analogous expression also applies to the secondary wave $I^{S2}(x,z)$ but with different values of κ_2 and σ_2. The complex wavenumbers $\kappa_1(x,z)$ and $\kappa_2(x,z)$ are defined by

$$\kappa(x,z) = k_f \sqrt{\mu(x,z)} = k_f \sqrt{1 + \left(\frac{ik_s z}{ik_f x - k_f L}\right)^{2/3}} \tag{19}$$

where the primary and secondary κ's and μ's are distinguished by particular choices of the

complex square and cube roots. These choices are summarized below

$$\begin{array}{ccc} -2\pi/3 < \arg(\mu_1) < 0 & ; & 0 < \arg(\mu_2) < 2\pi/3 \\ -\pi/3 < \arg(\kappa_1) < 0 & ; & 0 < \arg(\kappa_2) < \pi/3 \\ -\pi/2 < \arg(-\phi''(\kappa_1)/2) < \pi/2 & ; & -\pi < \arg(-\phi''(\kappa_2)/2) < 0 \ . \end{array} \tag{20}$$

Also included is the range of complex angles for the argument of $\phi''(\kappa)$ appropriate for (18). Finally, the values of $\sigma_1(x,z)$ and $\sigma_2(x,z)$ are either zero or one

$$\sigma(x,z) = \begin{cases} 1 & \text{for } \mathrm{Im}\{\phi(\kappa(x,z))\} > 0 \\ \\ 0 & \text{otherwise} \end{cases} \ , \tag{21}$$

which indicates whether or not the corresponding wave term contributes to the sum (15). The inclusion regions implied by (21) are indicated in Figure 3, downstream of the gray line A for the primary wave ($\sigma_1 = 1$), and downstream of the gray line B for the secondary wave ($\sigma_2 = 1$). These jumps in σ are responsible for the small discontinuities apparent in the displacement streamlines at lower altitudes.

The physical interpretation of the steepest descent formula (15) is that the buoyancy anomaly is composed of a ridge-symmetric part which is approximately the quasigeostrophic response, and asymmetric components which are primary and secondary wave fields characterized by complex wavenumbers κ_1 and κ_2. The primary wave field is analogous to Queney's (stationary phase) wave field since κ_1 approaches the stationary phase wavenumber (1947, equation 117 up to the substitution 114) in the downstream far-field. In addition, the far-field phaselines of constant $\mathrm{Im}\{\phi(\kappa_1)\}$, tilted upwards and upwind, coincide with the phase curves given in Queney (1948, equation 11).

A new feature from the steepest descent analysis is the secondary wave of complex wavenumber κ_2, which is an extremely weak contribution that is significant only very near the downstream surface. Two intriguing characteristics of the κ_2-wave are that its phaselines tilt upward and downstream, and that its maximum amplitude is located on the steepest part of the lee downslope. This reverse tilt of the waves is consistent with group velocities

that are upward, but downstream. Additionally, these waves are restricted to be below the gray line B in Figure 3, and are a near-inertial phenomenon with $\mathrm{Re}\{\kappa_2\} \approx k_f$. These facts suggest the interpretation that the secondary wave is generated at the surface, and is a scattered wave required to satisfy the downslope topographic boundary condition in the presence of the primary wave. It is however debatable whether this wave has much relevance beyond the scope of idealized linear wave models, since it is much weaker than the primary wave and strongly depends on the exact nature of the surface boundary condition. Nonetheless, it does represent direct analytical evidence for the generation of a secondary wave field through surface interactions.

Finally, Queney notes that the failure of the stationary phase method due aloft coincides with the divergence of the local wavenumber to infinity. In contrast, the steepest descent saddlepoint κ_1 (19) remains finite at the summit zenith and the local wavenumber (now complex) becomes near-inertial ($\mathrm{Re}\{\kappa_1\} \approx k_f$) slightly upstream of the ridge. Specifically, in the zenith direction ($x = 0$, large z) there is no breakdown of the steepest descent formulas, and an explicit approximation for the primary wave field (18) is obtained (for order-one $\mathcal{R}$ and smaller)

$$I^{S1}(0,z) \sim \sqrt{\frac{2\pi}{3}}\,(\mathcal{R}k_s z)^{\frac{1}{6}}\,\exp\left\{-\frac{3\sqrt{3}}{4}\left(\frac{k_s z}{\mathcal{R}^2}\right)^{\frac{1}{3}}\right\}\cos\left\{k_s z + \frac{3}{4}\left(\frac{k_s z}{\mathcal{R}^2}\right)^{\frac{1}{3}} - \frac{\pi}{12}\right\} \qquad (22)$$

which quantifies an unusually weak decay in the vertical. The significant feature in the above formula is the $z^{\frac{1}{3}}$ exponential decay which has the effect of making *the second e-folding height of wave amplitude eight times higher than the first.* This result, which cannot be derived by the stationary phase method, has also been verified with the direct quadrature of (9) and gives a very good approximation at heights above one wavelength ($\approx$ 6km). At the surface, the steepest descent approximation does recover the topographic buoyancy condition, but is weakly nonuniform as it does not imply correct values for the surface winds. However, since the original integral (4) is less singular when $z = 0$, special surface formulas can be derived. These are discussed in the next Section.

6. Near-Inertial Surface Waves & the QG Limit

Near-inertial oscillations of the surface ($z = 0$) winds in the lee of the ridge were analytically addressed in the Greens function analysis of Pierrehumbert (1984). For the along-ridge v-winds, the far-field upstream resembles a poleward geostrophic jet, whereas the far-field downstream displays ageostrophic oscillations whose amplitude decays as $x^{-1/2}$. In this Section, we present formulas for arbitrary topography that connect surface winds at finite Rossby number to zero Rossby number QG values.

At the surface ($z = 0$), the quasigeostrophic v-winds for flow past linearized topography $h(x)$ has the Fourier integral solution

$$v^{QG}(x,0) = -\,N\,\left\{\,\frac{1}{2\pi}\int_{-\infty}^{+\infty}\,\frac{|k|}{k}\;\mathrm{FT}[h(x)]\;e^{ikx}\;dk\,\right\} \tag{23}$$

where FT[$\cdot$] denotes the Fourier transform. The corresponding Fourier integral for Queney's linear model is

$$v(x,0) = -\,N\,\left\{\,\frac{1}{2\pi}\int_{-\infty}^{+\infty}\,\frac{|k|}{k}\;\mathrm{FT}[h(x)]\;\frac{k_f}{i\sqrt{k^2-k_f^2}}\;e^{ikx}\;dk\,\right\}\;. \tag{24}$$

However for the square root branch corresponding to (7), we have the fortuitous result

$$FT\,[\mathcal{H}(x)\,k_f\,J_0(k_f x)] = \frac{k_f}{i\sqrt{k^2-k_f^2}} \tag{25}$$

where $\mathcal{H}(\cdot)$ is the Heaviside step function and $J_0(\cdot)$ is a Bessel function of order zero. It follows from the Fourier convolution formula that

$$\mathrm{FT}[h(x)]\;\frac{k_f}{i\sqrt{k^2-k_f^2}}\;\;=\;\;\mathrm{FT}\left[\int_0^{+\infty}\,h(x-\tilde{x})\;k_f J_0(k_f\tilde{x})\;\;d\tilde{x}\right] \tag{26}$$

and by direct comparison it is seen that the integral (24) takes precisely the form of a QG solution (23) for a topography given by the equivalent wave topography $h^{eq}(x)$

$$h^{eq}(x) = \int_0^{+\infty}\,h(x-\tilde{x})\;k_f J_0(k_f\tilde{x})\;\;d\tilde{x}\;. \tag{27}$$

Figure 4 shows the equivalent topographies (units: H) for the bell-shaped ridge at $\mathcal{R} = 1$ and $\mathcal{R} = 1/3$ along with their surface v-winds (units: NH). In accordance with quasigeostrophic principles, poleward and equatorward jets are associated with upslopes and downslopes of $h^{eq}(x)$. Especially noteworthy is the singular way in which the quasigeostrophic limit is approached. In addition to the diminishing of wave amplitude, wavelength also shortens proportionally with the vanishing Rossby number. Lastly, note that the formula (27) is consistent with quasigeostrophy, since $k_f J_0(k_f x)$ integrates like a delta function in the zero Rossby number limit ($k_f \to \infty$).

By similar Fourier arguments, analogous expressions linking the finite Rossby number surface winds to QG v-winds can be obtained

$$\begin{aligned} u(x,0) &= -\int_0^{+\infty} v_x^{QG}(x-\tilde{x},0)\; k_f J_0(k_f \tilde{x})\;\; d\tilde{x} \\ v(x,0) &= \int_0^{+\infty} v^{QG}(x-\tilde{x},0)\; k_f J_0(k_f \tilde{x})\;\; d\tilde{x}\;. \end{aligned} \tag{28}$$

A by-product of above surface integrals are far-field ($x \to +\infty$) asymptotic formulas for the bell-shaped topography

$$\begin{aligned} u(x,0) &\sim \quad NH\;\; \mathcal{R}\, e^{-1/\mathcal{R}} \sqrt{\frac{2\pi}{k_f x}}\; \cos(k_f x - \pi/4) \\ v(x,0) &\sim -NH\;\; \mathcal{R}\, e^{-1/\mathcal{R}} \sqrt{\frac{2\pi}{k_f x}}\; \sin(k_f x - \pi/4) \end{aligned} \tag{29}$$

which recover the Greens function results of Pierrehumbert (1984) up to an extra factor of π that is the x-z area of the ridge (8). This explains the odd coincidence between the far-field results of Pierrehumbert (1984) and the asymptotics of the Bessel functions (Abramowitz & Stegun 1970).

A final connection to the Bessel functions involves the calculation of the wave drag (Bretherton 1969)

$$\mathcal{D} = \int_{-\infty}^{+\infty} p(x,0)\, h_x(x)\; dx = \frac{\rho_0\, U N}{\pi} \int_{k_f}^{+\infty} \sqrt{k^2 - k_f^2}\;\; \left|\hat{h}(k)\right|^2\;\; dk\;, \tag{30}$$

which is derived using the Fourier arguments of Blumen (1965). The integral formula (30) indicates the importance of wavenumbers above k_f in determining wave drag. As a consequence, in numerical computations of drag from surface pressure, it is imperative that these wavenumbers be handled accurately. However, for the special case of the bell-shaped ridge, this integral can be expressed using a modified Bessel function of order one (Smith 1979b, Gill 1982)

$$\mathcal{D} = \rho_0 \, UNH^2 \, \frac{\pi}{2\mathcal{R}} \, K_1\!\left(\frac{2}{\mathcal{R}}\right) \sim \rho_0 \, UNH^2 \, \frac{\pi}{4}\sqrt{\frac{\pi}{\mathcal{R}}} \, e^{-2/\mathcal{R}} \; . \tag{31}$$

along with an asymptotic approximation valid for small $\mathcal{R}$. As a result of the exponentially small Rossby number dependence, wave drag remains negligible until a sharp onset only after the Rossby number exceeds about 1/3 (Figure 5). Similar onsets are implied by the surface formulas (27,28).

7. Conclusions

Several new analytical results have been presented in this revisiting of Queney's problem at order-one Rossby number. Specialized quadratures for the rotating case have produced high-accuracy plots for anomalies in buoyancy, winds and vertical motion. By the nature of the desingularization procedure and the coordinate change (32), these quadratures maintain accuracy over a wide range of Rossby numbers. Directly above the ridge, a problematic region in Queney's analysis, an asymptotic formula for the unusual slow decay of the wave amplitude has been obtained (22) by the method of steepest descent. In addition, this analysis also suggests the existence of a weak back-scattered wave associated with the downslope. The singular nature of the QG limit to short wavelength waves has been illustrated via surface wind (29) and drag (31) formulas. Especially noteworthy is the onset appearance of waves with increasing Rossby number that is implied by these results.

One of the motivations of this work is to raise awareness of the discrepancies in Queney's streamline figure with rotation. The more important idea however is the notion that linear

topographic waves at finite Rossby number represent an intuitive intermediary between the non-rotating, hydrostatic and quasigeostrophic limits. This transition, from infinite to zero Rossby number, bridges the extremes from non-rotating waves concentrated aloft of the ridge, to quasigeostrophic, symmetric uplifting of isentropes. Although illustrated previously in Pierrehumbert (1986, Figure 21.5), and Trüb and Davies (Figures 5 and 7), this aspect bears reiteration. In terms of the buoyancy anomaly (Figure 6), these intermediate flows are characterized by the downstream dispersion of waves, whose surface signature has the inertial wavenumber. With decreasing Rossby number, these waves weaken and shorten, eventually giving way to the appearance of the symmetric, QG cold anomaly.

Acknowledgements

This work has benefited enormously from scientific discussions with and encouragement from R. Rotunno, J. Klemp and C. Snyder of the MMM group at NCAR Boulder. The author is also indebted to B. Alpert (NIST, Boulder) and M. Shelley (Courant Institute, NYU) for ideas and consultations on matters computational. Finally, the author thanks the late W. Blumen for making available Queney's 1947 manuscript, without which this work would not have been possible. The author acknowledges support through NSF DMR-9704724, NSERC RGPIN238928, and the Alfred P. Sloan Foundation.

Appendix A – Numerical Quadrature of the Fourier Integral

With the inertial singularity in the dispersion relation $m(k)$, the integrand (4) for $z > 0$ undergoes an infinite number of oscillations for k approaching k_f from above. Discrete numerical quadrature can result in aliasing errors which are manifested by the appearance of spurious waviness that is especially conspicuous in zero contours, or artifacts far upstream of the topography. Figures 1b and 2a-d have been computed using a *desingularized* trapezoidal rule which results in high-order (better than third-order in most cases) accurate schemes. The numerical methodology is based upon a singularity reduction strategy (Davis & Rabinowitz 1984, Section 3.3) and is illustrated here for the specific integral $I(x,z)$ (9).

First, a trigonometric change of variables is introduced to map the quadrature onto a finite interval

$$k = \begin{cases} k_f \cos\theta & \text{where} \quad -\dfrac{\pi}{2} \le \theta < 0 \quad \text{corresponds to} \quad 0 \le k < k_f \\ \\ k_f \sec\theta & \text{where} \quad 0 < \theta < \dfrac{\pi}{2} \quad \text{corresponds to} \quad k_f < k < +\infty \ , \end{cases} \tag{32}$$

which is motivated by the Queney analyses of (1947, 1960). The integrand in the θ-coordinate is plotted in Figure 7a for the location $(x,z) = (-200\pi, 4\pi)$. Explicitly shown is an example discretization of 200 points in the decay interval $(-\pi/2 < \theta < 0)$ and 400 points in the wave interval $(0 < \theta < \pi/2)$. At this location upstream and above the topography, the buoyancy anomaly ($b \approx -0.06$) is small by virtue of a nearly complete cancellation of the oscillatory quadrature. Numerical error due to loss of coherency of the type illustrated in the inset (Figure 7b) can ultimately lead to spurious waves in physical plots.

The basic idea for accurately evaluating the wave part of the integral

$$I_w(x,z) = k_f L \int_0^{\pi/2} \exp\{k_f(ix - L)\sec\theta\} \ \exp\{ik_s z \csc\theta\} \ \frac{\sin\theta}{\cos^2\theta} \ d\theta \tag{33}$$

is to decrease the amplitude of the rapid oscillations near the $\theta = 0^+$ endpoint. This can be

done through knowledge that the class of integrals

$$\mathcal{E}_n(k_s z) = \int_0^{\pi/2} \exp\{ik_s z \csc\theta\} \sin^n\theta \cos\theta \, d\theta \tag{34}$$

can be evaluated exactly via the recursion

$$\mathcal{E}_n(k_s z) = \begin{cases} \mathrm{Ei}(-ik_s z) & \text{for} \quad n = -1 \\ \\ e^{ik_s z} + \dfrac{ik_s z \, \mathcal{E}_{n-1}(k_s z)}{n+1} & \text{for} \quad n = 0, 1, 2 \ldots . \end{cases} \tag{35}$$

The index $n = -1$ integral is a special function called the *exponential integral* (Abramowitz & Stegun 1970)

$$\mathrm{Ei}(y) = \int_y^{\infty} \frac{\exp\{-u\}}{u} \, du \tag{36}$$

which can be accurately and efficiently evaluated by means other than direct quadrature. Combining (33) and (34) with $n = 1$ gives the integral relation

$$\begin{aligned} I_w(x,z) &= k_f L \exp\{k_f(ix - L)\} \mathcal{E}_1(k_s z) \\ &+ k_f L \int_0^{\pi/2} \mathcal{A}_w(\theta) \exp\{ik_s z \csc\theta\} \sin\theta \cos\theta \, d\theta \end{aligned} \tag{37}$$

where the amplitude function $\mathcal{A}_w(\theta)$

$$\mathcal{A}_w(\theta) = \sec^3\theta \exp\{k_f(ix - L)\sec\theta\} - \exp\{k_f(ix - L)\} \tag{38}$$

has a second-order zero at $\theta = 0$. With the higher-order zero at the singular endpoint, a trapezoidal rule quadrature of the de-singularized integral (37) is better than third-order accurate (Davis & Rabinowitz 1984, Section 2.9). Computations give an estimate of 3.6 for the rate of convergence; and only 400 points are required to eliminate the wavy artifacts from the zero contours.

Although unnecessary (since the infinite decay rates at $\theta = \pi/2$ do not introduce aliasing errors), a similar enhancement of accuracy is implemented for the decay part of the integral (9)

$$I_d(x,z) = -k_f L \int_{-\pi/2}^{0} \exp\{k_f(ix - L)\cos\theta\} \exp\{k_s z \cot\theta\} \sin\theta \, d\theta \, . \tag{39}$$

In this case, fourth-order accuracy is achieved for trapezoidal quadrature of the integral

$$\begin{aligned} I_d(x,z) &= \frac{k_f L}{k_s z - k_f(ix - L)} \\ &+ k_f L \int_{-\pi/2}^{0} \mathcal{A}_d(\theta)\ \exp\left\{[k_s z - k_f(ix-L)]\ \cot\theta\right\}\ \csc^2\theta\ \ d\theta \end{aligned} \tag{40}$$

since the amplitude function $\mathcal{A}_d(\theta)$

$$\mathcal{A}_d(\theta) = -\sin^3\theta\ \exp\left\{k_f(ix-L)\ (\cos\theta + \cot\theta)\right\} - 1 \tag{41}$$

also has a second-order zero at $\theta = -\pi/2$. For comparison, the integrands of the remaining quadratures in (37,40) are shown in Figure 8.

Minor variations on this desingularization scheme were used for the quadratures of w, u, v shown in Figures 2b-d. This approach also generalizes to arbitrary topography with sufficiently fast wavenumber decay. Note however that $\hat{h}(k)$ is required on a nonuniform distribution over wavenumber k (uniform in θ) and fast-Fourier methods cannot be used for the forward transform. Similar desingularization strategies apply to three-dimensional, linear flow around mountain topography, where both the nonrotating and rotating cases yield singular Fourier integrals. In the nonrotating case, Fourier quadratures for arbitrary three-dimensional topography have required unusually large discretizations to remove periodic and aliasing artifacts (Epifanio & Durran 2001).

Appendix B – The Steepest Descent Approximation

An asymptotic method described in many applied mathematical texts (Hinch 1991; Bender & Orszag 1978; Carrier et.al. 1966), the method of steepest descents is a generalization of the stationary phase method and is appropriate for Fourier-type integrals with complex exponential integrands. Deriving a steepest descent approximation involves two steps: changing the path of integration to the steepest descent path; and estimating the integral from endpoint/saddlepoint approximations, places where the exponential integrand is largest. The

steps for deriving the approximation (15) are outlined below, and assumes only a rudimentary background in complex function theory.

The focus of the method of steepest descent is the complex-valued exponent $\phi(k)$ as defined by (17) for the integral (9)

$$I(x,z) = \int_0^\infty e^{(ix-L)\,k}\; e^{i\,m(k)\,z}\; L\,dk = \int_{\mathcal{C}} e^{\phi(k)}\; L\,dk\;. \tag{42}$$

The standard complex path of integration $\mathcal{C}$ is shown in Figure 9a, where the passing of $\mathcal{C}$ below the branch point (indicated by B) at $k = k_f$ is determined by consistency between the complex branch choice (17) and the radiation condition (7). The key theorem from complex function theory is that the value of the integral (42) is the same for all paths that go from $k = 0$ to $k \to \infty$ and pass below the branch point singularity B. This path-independence allows the freedom to choose an equivalent path $\mathcal{C}'$ where the imaginary part (or phase) of $\phi(k)$ is a (piecewise) constant, and the integration reduces to the evaluation of an integral whose integrand is positive and real

$$\int_{\mathcal{C}} e^{\phi(k)}\; L\,dk \;\to\; e^{i\,\mathrm{Im}\{\phi(k)\}} \int_{\mathcal{C}'} e^{\,\mathrm{Re}\{\phi(k)\}}\; L\,dk\;. \tag{43}$$

In fact for the Queney problem, the new path $\mathcal{C}'$ consists of up to three sections, each with its own constant phase $\mathrm{Im}\{\phi(k)\}$ and results in the three-term approximation for $I(x,z)$ (15).

Grayscale contouring of $\mathrm{Re}\{\phi(k)\}$ is shown in Figures 9b-d for three illustrative values of (x,z). The axes are the real and imaginary parts of k. The darker shades indicate large negative values for $\mathrm{Re}\{\phi(k)\}$ where $e^{\,\mathrm{Re}\{\phi(k)\}}$ is exponentially small. The lighter shades indicate where the integrand is larger. The bold solid (zero phase) and dashed (positive phase) contours indicate steepest descent paths of constant $\mathrm{Im}\{\phi(k)\}$. The thick white line indicates the choice of the branch cut over which $(k-k_f)^{1/2}$ in $\phi(k)$ is discontinuous (17). Over the full range of x and positive z, there are three cases to consider. This distinction leads to the identification of the upstream, aloft and downslope regions of Figure 3.

For the first step, there are three distinct cases for defining the path of steepest descent $\mathcal{C}'$. In the upstream case (Figure 9b: $x = -400$km, $z = 3$ km), the steepest descent path $\mathcal{C}'$

is from the origin A to ∞_1 and follows the zero phase contour (bold solid line). This path can be reconnected with the positive real k-axis (the original ∞ in Figure 9a) at large values of $|k|$ where e^{ϕ} is exponentially small (darker shading), and so does not contribute to the integral. Note that the largest contribution of the integral will be from the vicinity of $k = 0$ (lighter shading). For larger values of x and aloft of the mountain (Figure 9c: $x = 100$km, $z = 3$ km), the zero phase path from the origin A now leads to the branch point B (where e^{ϕ} goes to zero). The integration is then continued along a different constant phase path from B through S_1 to ∞_1. The exponent $\mathrm{Re}\{\phi(k)\}$ is again largest near $k = 0$, but also achieves a local maximum at the saddlepoint S_1 (which must also be a crossing point of equi-phase contours). The saddlepoint condition for the location $k = \kappa_1$ of S_1 is $\phi'(\kappa_1) = 0$. Finally in the downslope case (Figure 9d: $x = 100$km, $z = 3$ km), the steepest descent path $\mathcal{C}'$ follows the course: A, ∞_2, S_2, B, S_1, ∞_1 where the new saddlepoint S_2 is also a local maximum of $\mathrm{Re}\{\phi(k)\}$.

The second step estimates the most significant contributions to the integral (42) along the path $\mathcal{C}'$ from locations where the exponent $\mathrm{Re}\{\phi(k)\}$ has local maxima. For the three cases (Figures 9b-d), the three possible contributions come from: the endpoint A ($k = 0$), and the saddlepoints S_1 and S_2. These correspond to the three terms defined in (15). Local to the endpoint A, the approximation I^{QG} (16) is obtained by replacing $\phi(k)$ with its linear Taylor series and integrating from $k = 0 \to \infty$ (any direction where the integral converges gives the same result)

$$I^{QG}(x,z) \approx \int_0^\infty e^{\phi'(0)\,k}\; L\,dk = -\frac{L}{\phi'(0)} = \frac{k_f L}{k_s z - k_f(ix - L)}\ . \tag{44}$$

Local to a saddlepoint S, the approximation I^S (18) is obtained by replacing $\phi(k)$ with its quadratic Taylor approximation at $k = \kappa$ and integrating along any line $\mathcal{L}$ over which the

integral converges

$$\begin{aligned} I^S(x,z) &\approx e^{\phi(\kappa)} \int_{\mathcal{L}} e^{\,\phi''(\kappa)\,(k-\kappa)^2/2}\; L\,dk \\ &= \sqrt{\frac{2\pi L^2}{|\phi''(\kappa)|}}\; \exp\{\,\phi(\kappa) - i\,\arg(-\phi''(\kappa)/2)\}\;\; . \end{aligned} \tag{45}$$

The linear Taylor term is absent because of the saddlepoint criterion $\phi'(\kappa) = 0$, which can be used to obtain (19) as well as the simplified forms

$$\phi(\kappa) = \frac{(ix - L)\kappa^3}{k_f^2} \qquad ; \qquad \phi''(\kappa) = \frac{3(ix - L)\kappa}{\kappa^2 - k_f^2} \tag{46}$$

for use in the steepest descent formula (45). The estimation of the integral by saddlepoints fails only at the surface $z = 0$ where the saddlepoints are degenerate with the branch point. In the case of the buoyancy integral, the saddlepoint contributions happen to be zero so that this degeneracy is of no consequence. Applying steepest descent to the u or v winds however is invalid at $z = 0$.

More generally, path-independence of the integral (10) requires only that the integrand be an analytic function (excepting the branch cut), and so will hold for a broad class of topographies $h(x)$. It seems however that a generic feature of such analyses will be the characterization of the solution into quasigeostrophic, primary and secondary wave contributions.

References

Abramowitz M. & I.A. Stegun, 1970: Handbook of Mathematical Functions. National Bureau of Standards, 1046pp.

Bender C.M. & S.A. Orszag, 1978: Advanced Mathematical Methods for Scientists and Engineers. McGraw-Hill, 593pp.

Blumen, W., 1965: Momentum flux by mountain waves in a stratified atmosphere. *J. Atmos. Sci.*, **22**, 529-534.

Bretherton, F.P., 1969: Momentum transport by gravity waves. *Quart. J. Roy. Meteor. Soc.*, **95**, 213-243.

Carrier G.F., M. Krook & C.E. Pearson, 1966: Functions of a Complex Variable. McGraw-Hill, 438pp.

Davis, P.J. & P. Rabinowitz, 1984. Methods of Numerical Integration. Academic Press, 612pp.

Epifanio, C.C. & D.R. Durran, 2000: Lee vortex formation in free-slip stratified flow over ridges. Part I: Comparison of weakly nonlinear inviscid theory and fully nonlinear viscous simulations. *J. Atmos. Sci.*, submitted.

Garner, S.T., 1999: Blocking and frontogenesis by two-dimensional terrain in baroclinic flow. Part II: Analysis of flow stagnation mechanisms. *J. Atmos. Sci.*, **56**, 1509-1523.

Gill, A.E., 1982: Atmosphere-Ocean Dynamics. Academic Press, 662pp.

Hinch, E.J., 1991: Perturbation Methods. Cambridge Press, 160pp.

Hsu, W.-R. & W.-Y. Sun, 2001: A time-split, forward-backward numerical model for solving a nonhydrostatic and compressible system of equations. *Tellus*, **53A**, 297-299.

Klemp, J.B. & D.R. Durran, 1983: An Upper boundary condition permitting internal gravity

wave radiation in numerical mesoscale models. *Mon. Wea. Rev.* **111**, 430-444.

Pierrehumbert, R.T., 1984: Linear results on the barrier effects of mesoscale mountains. *J. Atmos. Sci.* **41**, 1356-1367.

Queney, P., 1960: Dynamic Meteorology, ed P. Morel. D. Reidel Publishing Company, 622pp.

Queney, P., 1948: The problem of air flow over mountains: A summary of theoretical results, *Bull. AMS* **29**, 16-26.

Queney, P., 1947: Theory of perturbations in stratified currents with application to airflow over mountain barriers. Department of Meteorology, University of Chicago, Misc. Rep. No 23, 67pp.

Smith, R.B., 1979a: The influence of mountains on the atmosphere. *Advances in Geophysics*, Vol. 21, Academic Press, 87-230.

Smith, R.B., 1979b: The influence of the Earth's rotation on mountain wave drag. *J. Atmos. Sci.*, **36**, 177-180.

Smith, R.B., 1982: Synoptic observations and theory of orographically disturbed wind and pressure. *J. Atmos. Sci.*, **39**, 60-70.

Trüb, J. & H.C Davies, 1995. Flow over a mesoscale ridge: Pathways to regime transition. *Tellus* **47A**, 502-524.

Figure Captions

Figure 1: Comparison of displacement streamlines from: (a) Queney (1948, p22), and (b) numerical quadrature of the Fourier integral (9). The streamlines (13) are shown as thick dark lines (for z^∞ at intervals of $\pi/4$). Also shown are the undisturbed streamlines (thin) and phaselines of zero vertical displacement (dashed).

Figure 2: Contours of (a) buoyancy anomaly b, (b) vertical motion w, (c) across-ridge disturbance winds u and (d) along-ridge winds v from direct Fourier quadratures with $\mathcal{R} = 1$. Positive and zero contours are solid, negative contours are dashed. Topography corresponding to $\mathcal{F} = 3$ is indicated in shaded gray.

Figure 3: Displacement streamlines from steepest descent approximation. The streamlines (10), shown as thick dark lines, correspond to the same values as in Figure 1. Also shown are the undisturbed streamlines (thin) and phaselines of zero vertical displacement (dashed). The gray lines demarcate the upstream, aloft and downslope regimes of the steepest descent theory.

Figure 4: Surface topography $h(x)$ and quasigeostrophic ($\mathcal{R} = 0$) surface v-winds for the bell-shaped topography (8) are shown by gray lines. For Rossby numbers $\mathcal{R} = 1$ (solid) and $\mathcal{R} = 1/3$ (dashed), the surface v-winds (24) implied by $h(x)$ are exactly the quasigeostrophic v-winds corresponding to the $h^{eq}(x)$ topographies (27).

Figure 5: Wave drag (units: ρUNH^2) versus Rossby number.

Figure 6: Buoyancy anomaly as in Figure 2a, but for varying mountain widths (a) $L = 50$km ($\mathcal{R} = 2$) and (b) $L = 200$km ($\mathcal{R} = 1/2$).

Figure 7: (a) Plot of the integrands of $I_d(\theta)$ (39) and $I_w(\theta)$ (33) for a location $(x, z) = (-200\pi, 4\pi)$ that is upstream and above the ridge. (b) Close-up of the discretization near the inertial singularity showing loss of coherency of the oscillations in the integrand.

Figure 8: (a) Plot of the desingularized integrands of (40) and (37) for the same location as in Figure 6. (b) Close-up of the discretization near the inertial singularity shows the diminished amplitude of the oscillations approaching the inertial singularity.

Figure 9: Integration paths in complex k-space for Fourier inversion (4): (a) standard integration path for Fourier inversion following Queney (1947); steepest descent paths for (b) upstream, (c) aloft and (d) downslope regions.

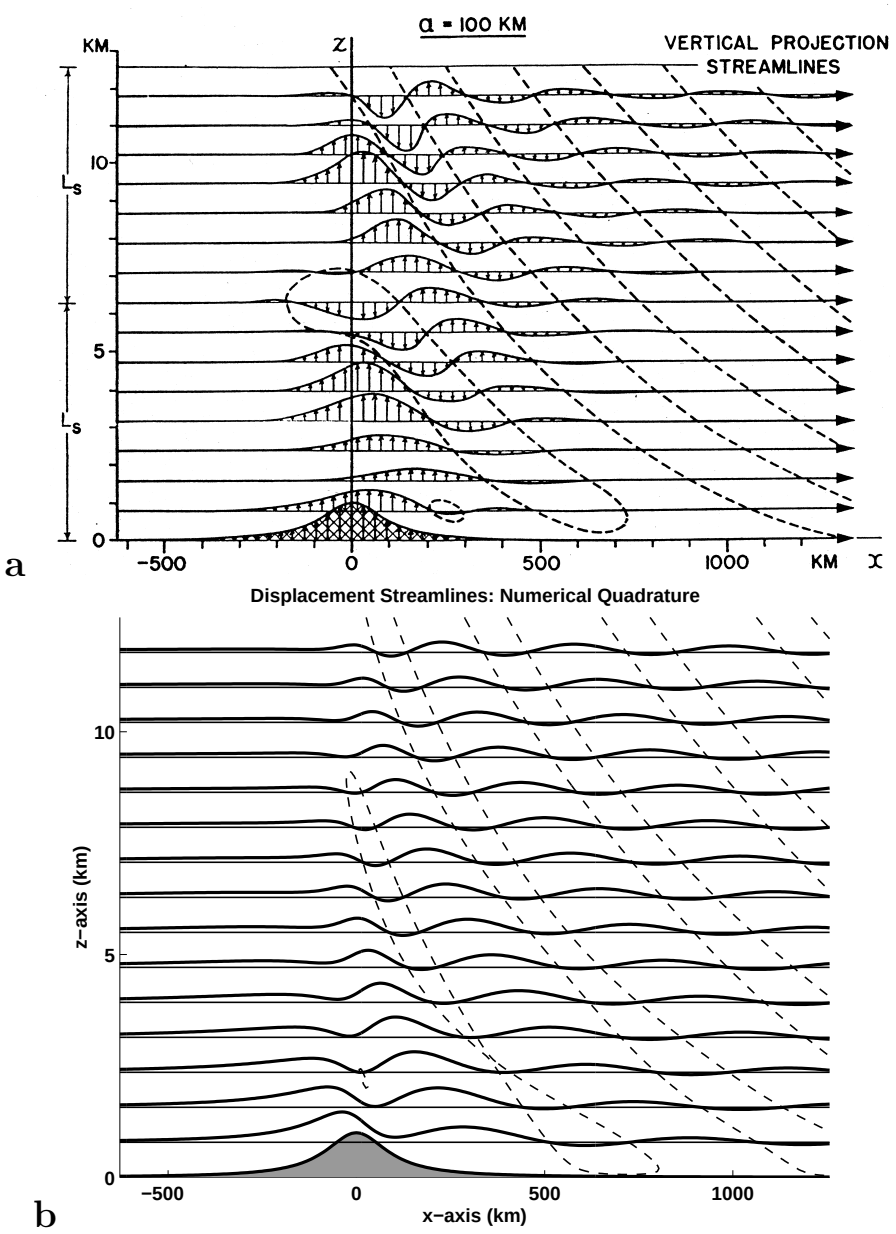

Figure 1: Comparison of displacement streamlines from: (a) Queney (1948, p22), and (b) numerical quadrature of the Fourier integral (9). The streamlines (13) are shown as thick dark lines (for z^∞ at intervals of $\pi/4$). Also shown are the undisturbed streamlines (thin) and phaselines of zero vertical displacement (dashed).

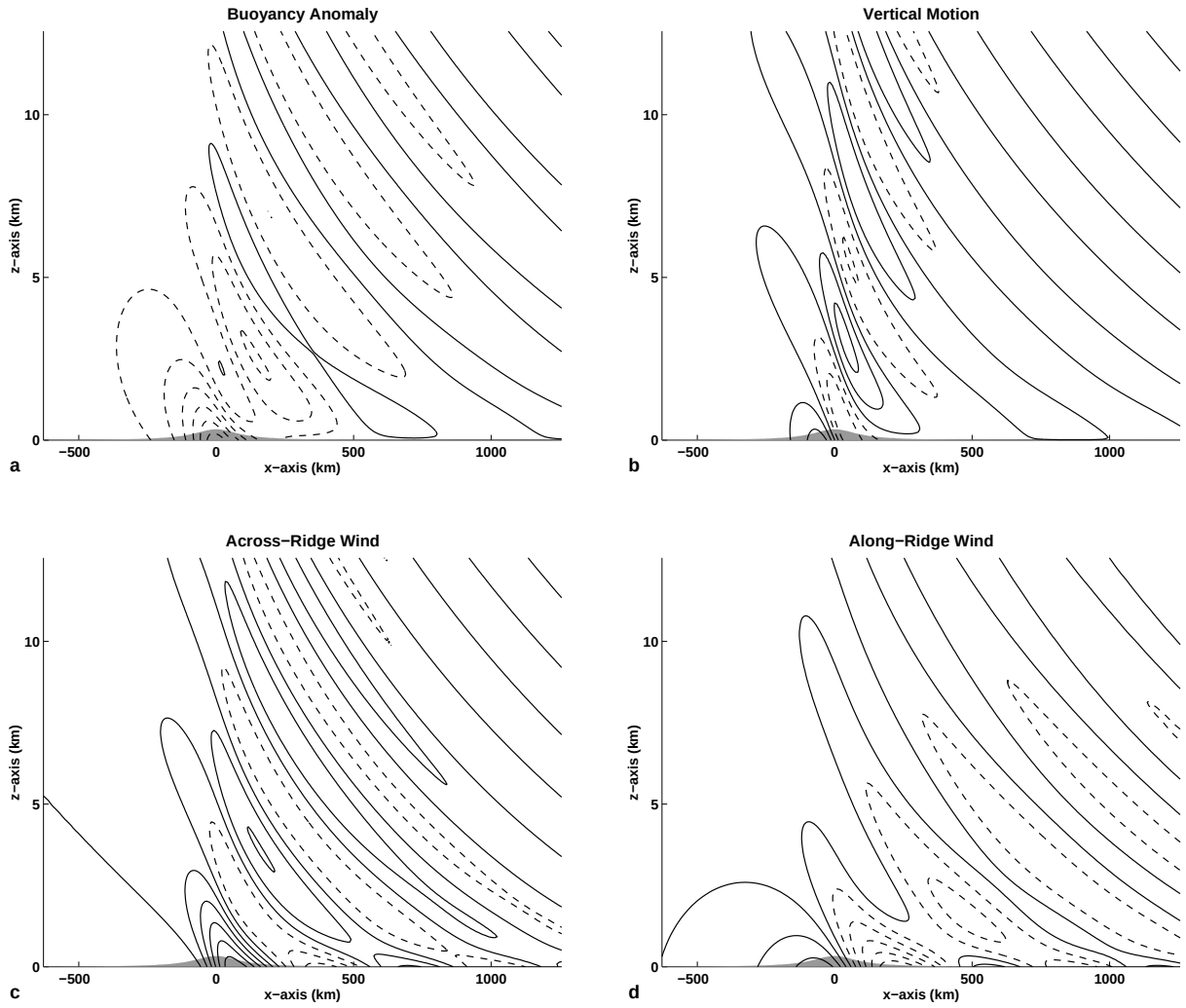

Figure 2: Contours of (a) buoyancy anomaly b, (b) vertical motion w, (c) across-ridge disturbance winds u and (d) along-ridge winds v from direct Fourier quadratures with $\mathcal{R} = 1$. Positive and zero contours are solid, negative contours are dashed. Topography corresponding to $\mathcal{F} = 3$ is indicated in shaded gray.

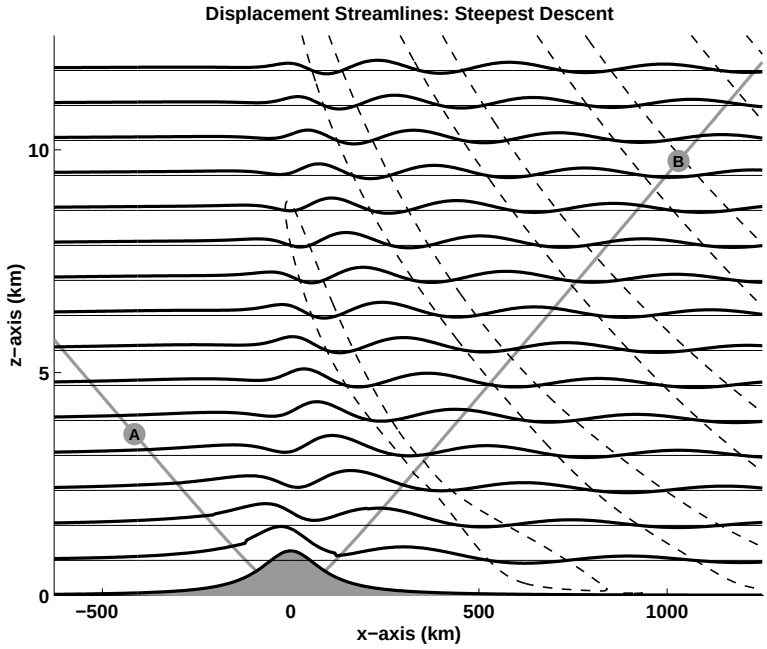

Figure 3: Displacement streamlines from steepest descent approximation. The streamlines (10), shown as thick dark lines, correspond to the same values as in Figure 1. Also shown are the undisturbed streamlines (thin) and phaselines of zero vertical displacement (dashed). The gray lines demarcate the upstream, aloft and downslope regimes of the steepest descent theory.

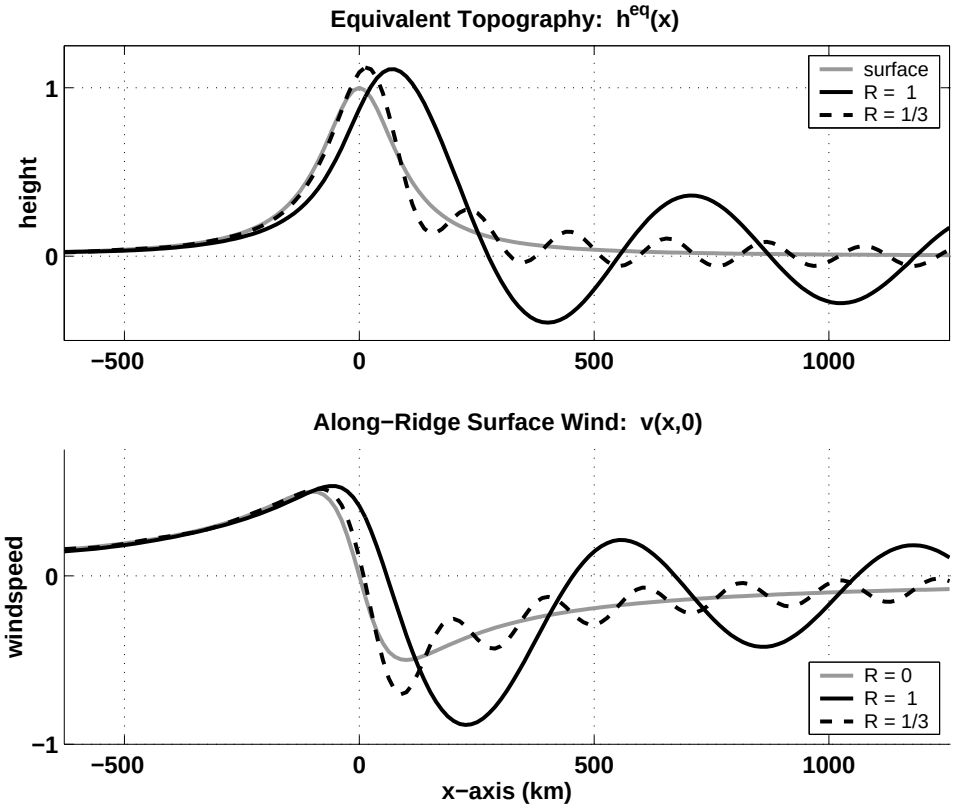

Figure 4: Displacement streamlines from steepest descent approximation. The streamlines (10), shown as thick dark lines, correspond to the same values as in Figure 1. Also shown are the undisturbed streamlines (thin) and phaselines of zero vertical displacement (dashed). The gray lines demarcate the upstream, aloft and downslope regimes of the steepest descent theory.

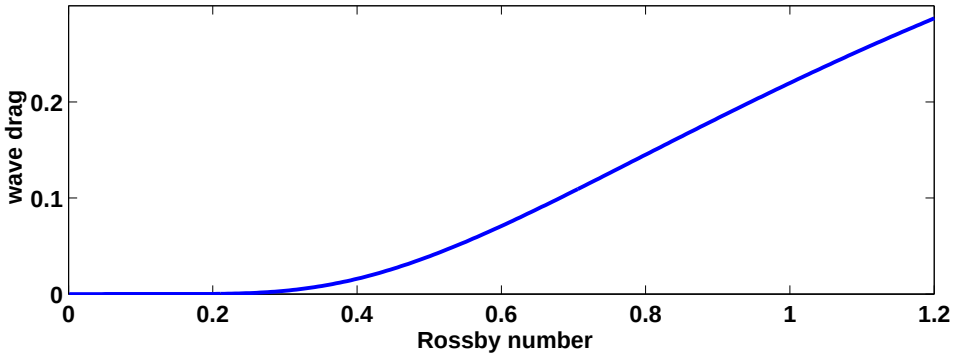

Figure 5: Wave drag (units: ρUNH^2) versus Rossby number.

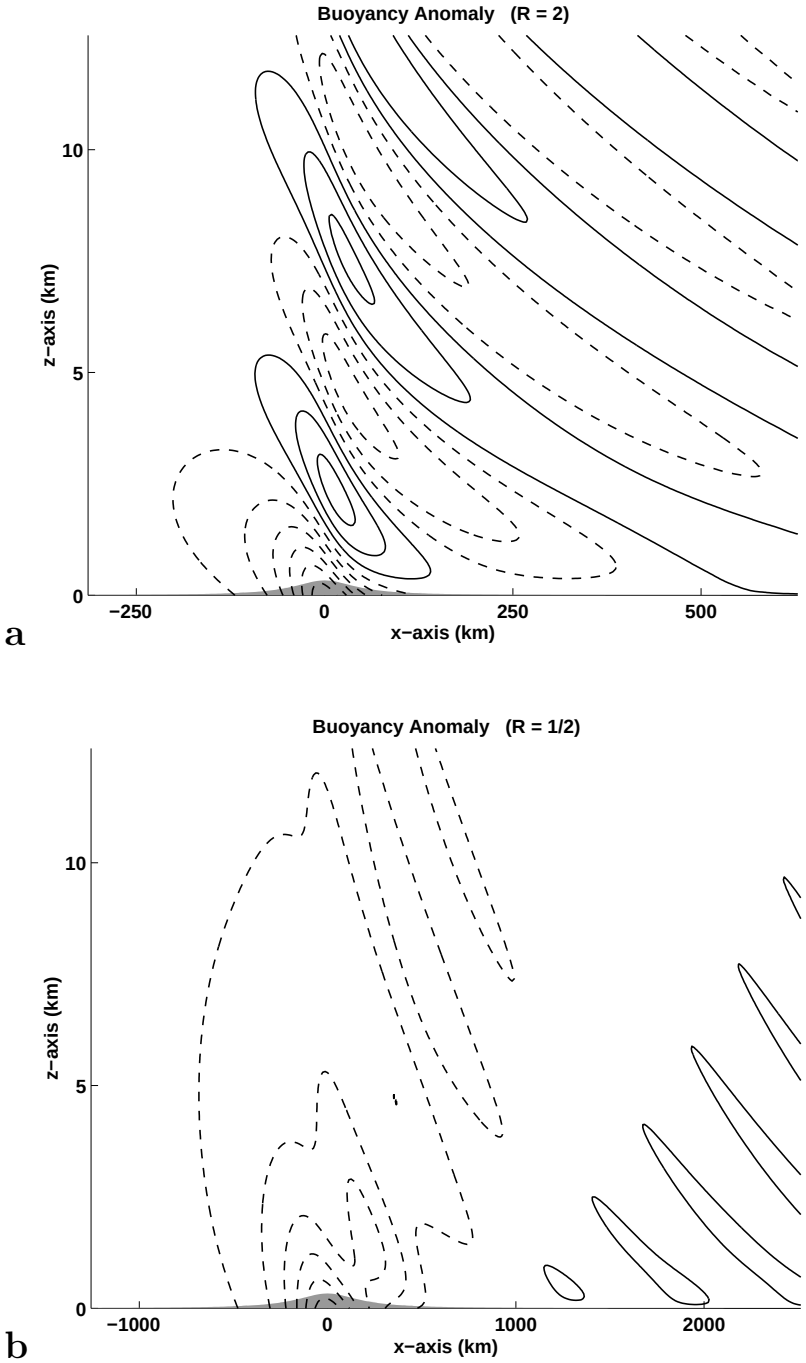

Figure 6: Buoyancy anomaly as in Figure 2a, but for varying mountain widths (a) $L = 50$km ($\mathcal{R} = 2$) and (b) $L = 200$km ($\mathcal{R} = 1/2$).

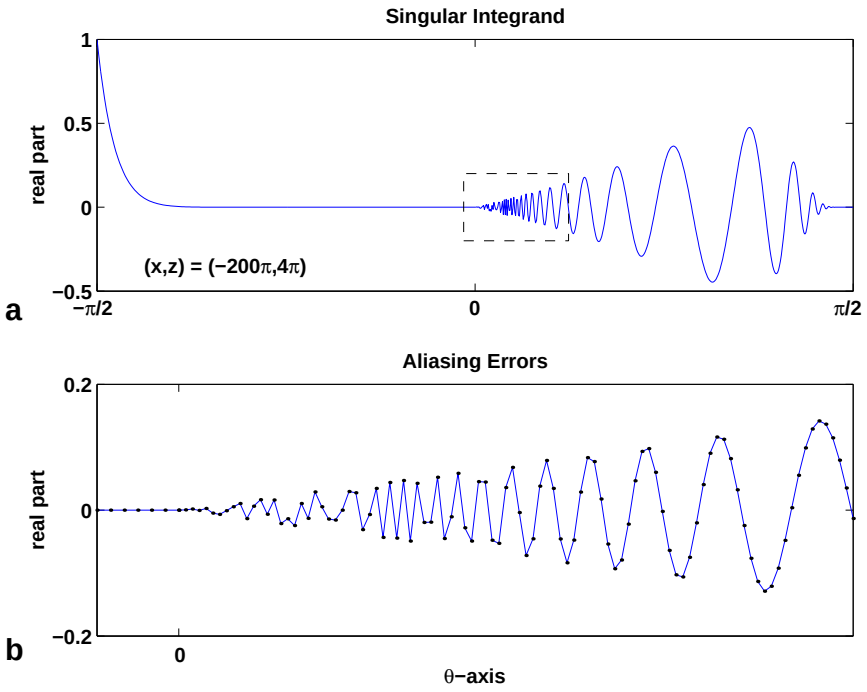

Figure 7: (a) Plot of the integrands of $I_d(\theta)$ (39) and $I_w(\theta)$ (33) for a location $(x, z) = (-200\pi, 4\pi)$ that is upstream and above the ridge. (b) Close-up of the discretization near the inertial singularity showing loss of coherency of the oscillations in the integrand.

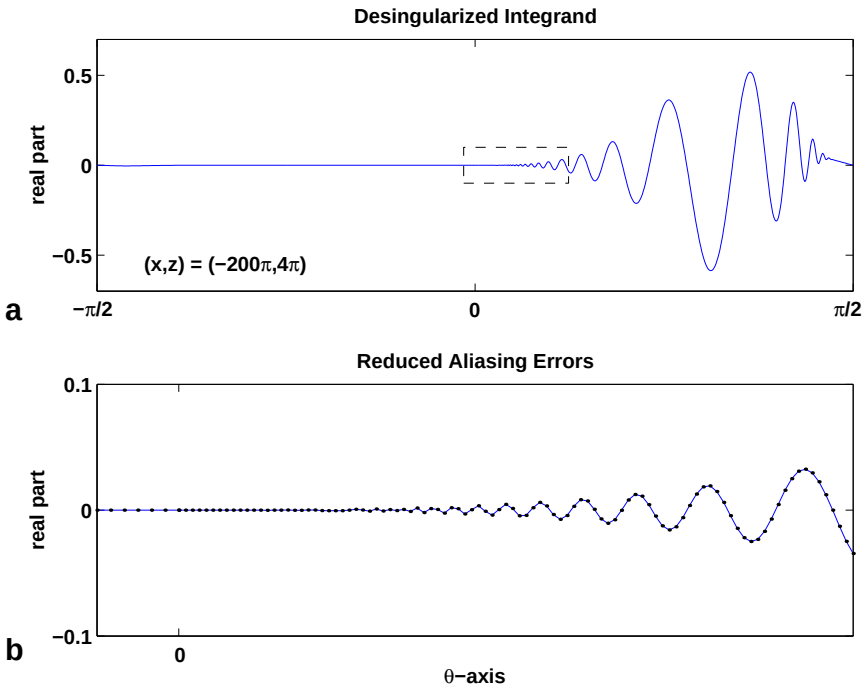

Figure 8: (a) Plot of the desingularized integrands of (40) and (37) for the same location as in Figure 6. (b) Close-up of the discretization near the inertial singularity shows the diminished amplitude of the oscillations approaching the inertial singularity.

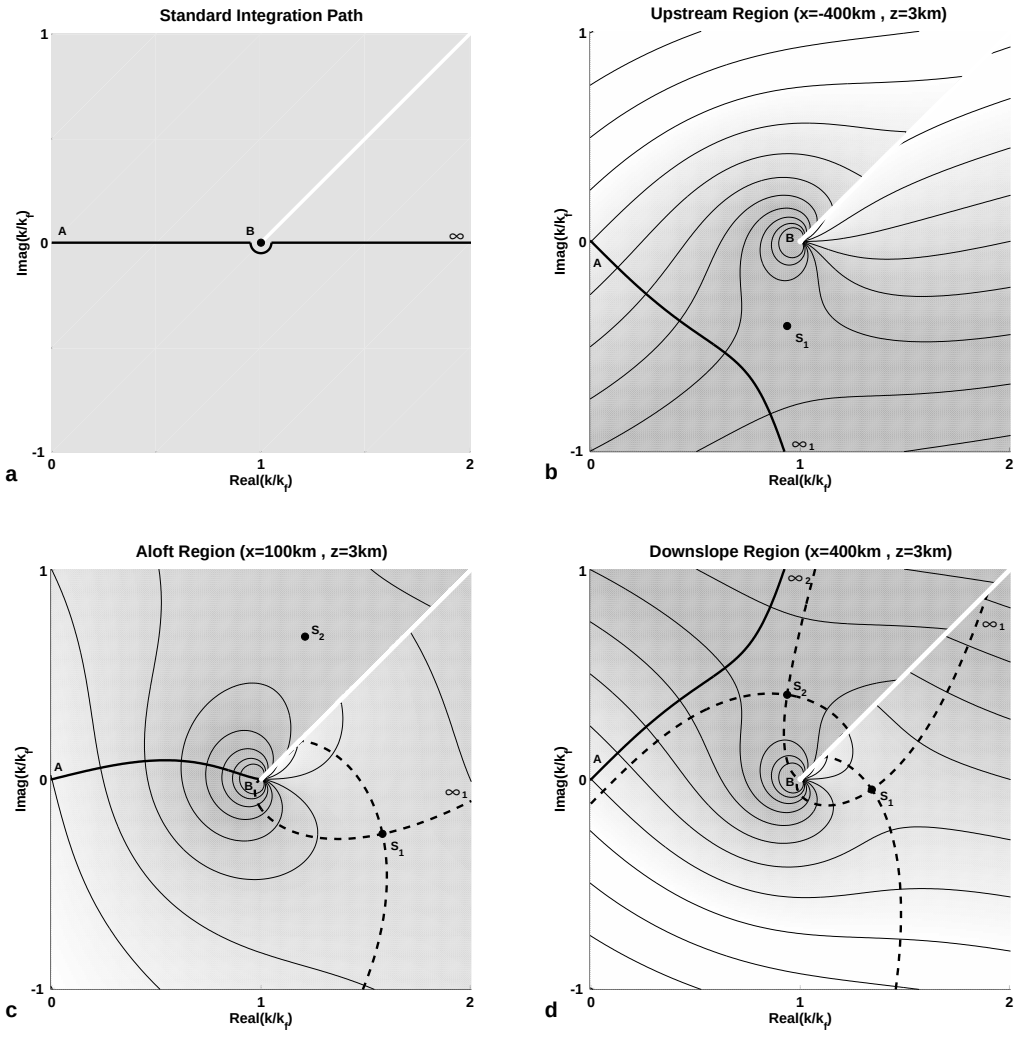

Figure 9: Integration paths in complex k-space for Fourier inversion (4): (a) standard integration path for Fourier inversion following Queney (1947); steepest descent paths for (b) upstream, (c) aloft and (d) downslope regions.